



CHALMERS
UNIVERSITY OF TECHNOLOGY

High Li⁺ and Na⁺ Conductivity in New Hybrid Solid Electrolytes based on the Porous MIL-121 Metal Organic Framework

Downloaded from: <https://research.chalmers.se>, 2021-08-31 11:36 UTC

Citation for the original published paper (version of record):

Zettl, R., Lunghammer, S., Gadermaier, B. et al (2021)

High Li⁺ and Na⁺ Conductivity in New Hybrid Solid Electrolytes based on the Porous MIL-121 Metal Organic Framework

Advanced Energy Materials, In Press

<http://dx.doi.org/10.1002/aenm.202003542>

N.B. When citing this work, cite the original published paper.

High Li⁺ and Na⁺ Conductivity in New Hybrid Solid Electrolytes based on the Porous MIL-121 Metal Organic Framework

Roman Zettl, Sarah Lunghammer, Bernhard Gadermaier, Athmane Boulaoued, Patrik Johansson, H. Martin R. Wilkening,* and Ilie Hanzu*

Solid-state electrolytes (SSEs) can leapfrog the development of all-solid-state batteries (ASSBs), enabling them to power electric vehicles and to store renewable energy from intermittent sources. Here, a new hybrid Li⁺ and Na⁺ conducting SSE based on the MIL-121 metal-organic framework (MOF) structure is reported. Following synthesis and activation of the MOF, the free carboxylic units along the 1D pores are functionalized with Li⁺ or Na⁺ ions by ion exchange. Ion dynamics are investigated by broadband impedance spectroscopy and by ⁷Li and ²³Na NMR spin-lattice relaxation. A crossover at 50 °C (Li⁺) and at 10 °C (Na⁺) from correlated to almost uncorrelated motion at higher temperature is observed, which is in line with Ngai's coupling model. Alternatively, in accordance to the jump relaxation model of Funke, at low temperature only a fraction of the jump processes are successful as lattice rearrangement in the direct vicinity of Li⁺ (Na⁺) is slow. ¹H NMR unambiguously shows that Li⁺ is the main charge carrier. Conductivities reach 0.1 mS cm⁻¹ (298 K, Na⁺) while the activation energies are 0.28 eV (Li⁺) and 0.36 eV (Na⁺). The findings pave the way towards development of easily tunable and rationally adjustable high-performance MOF-based hybrid SSEs for ASSBs.

1. Introduction

Advanced batteries are of high importance in many technological fields.^[1,2,3] They take advantage of manifold electrode materials,^[4] liquid and solid-state (ceramic and polymeric) electrolytes (SSE)^[1,5–10] as well as small ionic charge carriers such as Li⁺, Na⁺, and others.^[11,12] From small portable electronics to much larger implementations such as electric vehicles and grid-relevant batteries^[13] for renewable energy storage, there is a constant need for improvement with respect to technical performance and costs.^[3] The resurgence of Na-ion battery research, after being quasi-abandoned following the successful commercialization of Li-ion batteries (LIBs), is a clear expression of the current strive for alternative, efficient, and cost-effective energy storage solutions.^[14] Currently, we see significant efforts aimed at replacing the conventional liquid


electrolytes by SSEs to create practical all-solid-state batteries (ASSBs).^[5,15] Not only are they perceived as safer, but they are also expected to enable the use of metallic negative electrodes (and hence lithium metal batteries (LMBs)),^[9,16,17] which would significantly increase the energy density of the battery cells.^[16]

While SSEs certainly are game-changing materials, finding a successful SSE is a complex and challenging task.^[5,6] Some key features of a good solid electrolyte for both LIBs and LMBs include: i) high ionic conductivity at ambient and sub-ambient temperature, ii) appreciable Li⁺ transference number, iii) thermal and electrochemical stability, iv) compatibility with electrodes, v) good electronic insulating properties, vi) mechanical strength, and vii) environmental friendliness. Hardly can one material concomitantly meet the high ionic conductivity and the good (electro)chemical stability requirements, let alone the other criteria above. In fact, it seems that, more often than not, SSEs are unstable in contact with the active materials.^[9,17,18] Nevertheless, it was very recently shown that the relation between redox activity and electrochemical stability is complex. Sometimes, the electrochemical stability window is probably wider than what could be expected from first principle thermodynamic calculations.^[19] Thus, the main hurdle remains the ion transport itself—a solid-state electrolyte (SSE) with an ionic conductivity

Dr. R. Zettl, Dr. S. Lunghammer, B. Gadermaier,
Prof. H. M. R. Wilkening, Dr. I. Hanzu
Institute of Chemistry and Technology of Materials
Graz University of Technology (NAWI Graz)
Stremayrgasse 9, Graz 8010, Austria
E-mail: wilkening@tugraz.at; hanzu@tugraz.at

Dr. A. Boulaoued, Prof. P. Johansson
Department of Physics
Chalmers University of Technology
Gothenburg 412 96, Sweden

Prof. P. Johansson, Prof. H. M. R. Wilkening, Dr. I. Hanzu
Alistore-ERI European Research Institute
CNRS FR3104
Hub de l'Energie
Rue Baudelocque, Amiens F-80039, France

 The ORCID identification number(s) for the author(s) of this article can be found under <https://doi.org/10.1002/aenm.202003542>.

© 2021 The Authors. Advanced Energy Materials published by Wiley-VCH GmbH. This is an open access article under the terms of the Creative Commons Attribution-NonCommercial-NoDerivs License, which permits use and distribution in any medium, provided the original work is properly cited, the use is non-commercial and no modifications or adaptations are made.

DOI: 10.1002/aenm.202003542

similar to that of liquid electrolytes is very rare, although there are some serious and plausible contenders.^[5,6,8,12]

Metal–organic frameworks (MOFs) are a class of inorganic–organic hybrid crystalline materials, also called coordination polymers.^[20,21] They are extended arrays composed of isolated metal atoms, also termed nodes, that are connected by organic ligands, called linkers. MOFs can extend in one, two, or three dimensions; many of these materials have well-defined pores. MOFs have a wide range of (industrial) applications including gas storage and separation, molecular recognition, nonlinear optics, heterogenous catalysis, and many others.^[20] Judicious ligand choice allows for custom design of pore size and geometry—the possibilities are truly enormous and the many unique properties of MOFs can be tuned by this approach. Apart from the pore size and geometry, also physical and chemical properties such as electrical conductivity, magnetic behavior, reactivity, Lewis acid–base properties can be tuned by the choice of both metal centers and linkers. MOFs are in fact becoming a fertile ground for a broad spectrum of functional materials development, including the nascent field of MOF-based ion conductors.^[10,22]

Hitherto, few publications have reported on MOFs with Li⁺ conducting properties.^[23–25] Several approaches are, however, known to realize MOF ion conductors. One possibility is to do a full post-synthetic modification. Following the successful synthesis of a known MOF, a new lithium-bearing functionality is grafted. For instance, lithium alkoxides were grafted on two different MOF structures resulting in Li⁺ conductivity.^[23] The bulky aliphatic part of the secondary or tertiary alkoxide shields the negative charge and thus weakens the alkoxide–Li⁺ interaction. The post modification, however, may involve tedious synthesis procedures. Another possibility is to immobilize the anions of a lithium salt so that the MOF becomes a Li⁺ single ion conductor. This can be achieved by a covalently bound anion within the MOF structure^[25] or by having a strong Coulomb interaction between the anion and the MOF framework.^[24,26] Indeed, the electron-unsaturated MOF metal centers may lead to strong coordination of anions of a lithium salt.^[24] Alternately, an anion coordinating structure can be grafted onto the organic linker.^[27] One common property of this kind of conductors is that they all require the presence of a liquid solvent or a small molecule confined within the pores to facilitate the ion transport. Due to the geometry and the large size of the pores, the ion conduction is significantly slower in the absence of a mobile solvent. Thus, they are probably better categorized as hybrid SSEs, with a similar relation that gel polymer electrolytes (GPEs) have versus solid polymer electrolytes. However, unlike Li⁺-conducting GPEs, MOF ion conductors are, from a rheological point of view, true solids.

Here, we report on a new MOF-based SSE based on the MIL-121 structure.^[28] In the following, we call the MOF-based electrolyte developed a solid electrolyte; strictly speaking it is a hybrid liquid–solid electrolyte. The electrolyte prepared is, however, a “dry” powder, it has no waxy texture as one might assume. Our study demonstrates a versatile, tunable route to easily prepare ion conductors for Li⁺, Na⁺ and possibly also for other metal cations of interest.^[29] The MIL-121 structure is flexible and consists of aluminum centers that are linked by pyromellitic acid (1,2,4,5-benzenetetracarboxylic acid) units (**Figure 1**).

Out of the four carboxylic units of the linker, only two are used for building the framework. The others are free and the protons of these carboxylic units can be exchanged by lithium or sodium ions that give the MOF new ion conduction functionality. To our knowledge, this is, however, the first report using MIL-121 to form a hybrid lithium and sodium SSE system.

Overall, we hereby present structural, conductive, and diffusion properties of the new Li⁺ and Na⁺ SSEs made from MIL-121, shedding light on the relation between the macroscopic performance and its structural and ion dynamics properties.

2. Results and Discussion

2.1. Post-Synthetic Modifications of MIL-121

Prior to studying ionic conductivities and self-diffusion properties of our materials, we analyzed the influence of different post-synthetic modifications of MIL-121 by X-ray powder diffraction (XRD). In **Figure 2**, the pattern of pristine MIL-121 is compared to those of the modified MIL-121 samples obtained via the different approaches. While **Figure S1** in the Supporting Information provides the corresponding scanning electron microscopy (SEM) images, **Figure S2** in the Supporting Information shows XRD patterns to study the thermal and mechanical stability of MIL-121.

Through lithiation with 1 M LiOH, we obtained an X-ray amorphous material with no sharp reflections seen in the pattern. Likely, the reason for the collapse of the structure was the high pH of LiOH. A second attempt with LiOH was realized with only 0.1 M LiOH solution, which was added in small portions while the pH was controlled throughout the experiment in order to keep the pH value below 10. This titration approach led to an XRD pattern much closer to that of pristine MIL-121. We observed that intensities of the reflections are different but crystallinity could still be maintained. The main reflections occur at similar positions on the 2θ scale as for the pristine material. Continuing from that, we chose lithium acetate (LiAc), yielding a much lower pH-value than LiOH, to lithiate MIL-121. Here, the obtained pattern shows that this approach led to a modified MIL-121 sample with higher crystallinity than the prior approaches using LiOH. Reflections occur at slightly different positions which we explain through different strains generated in the crystal lattice of the material caused by the exchange of H⁺ with Li⁺ at the COOH-groups in MIL-121. Since lithiation with LiAc was simpler, as it required no pH control and led to a well-crystalline material, we decided to perform sodiation with sodium acetate (NaAc) on MIL-121 (see pattern at the top of **Figure 2**). As compared with MIL-121/Li (LiAc), XRD clearly revealed that a less crystalline sample was obtained. Nevertheless, the main reflections were detected at the same positions as for pristine MIL-121. In general, broadening of the X-ray reflections is due to grain sizes and strain introduced. Here, XRD revealed distinct changes in long-range crystallinity of the two samples; in the case of MIL-121/Na (NaAc) the pattern resembles that of a nanostructured sample that is, most likely, further affected by strain effects. Such effects also emerge after the MIL-121 was exposed to pressure, see **Figure S2** in the Supporting Information.

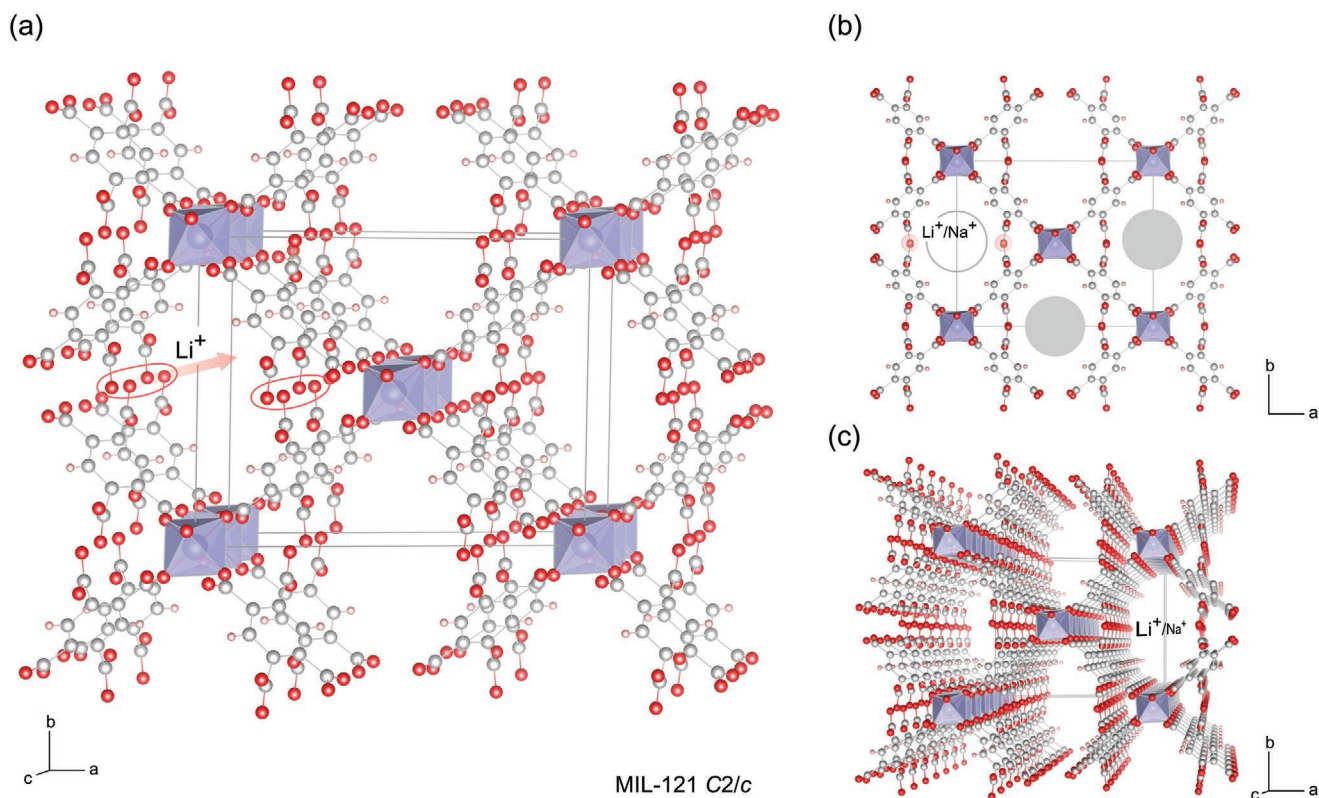


Figure 1. a) Crystal structure of MIL-121 with the ion pathways indicated by an arrow pointing toward the c -direction. The aluminum centers are coordinated by 1,2,4,5-benzenetetracarboxylic acid (also known as pyromellitic acid). Only two of the carboxylic units are bound to the aluminum centers, the others are free and form chains along the walls of 1D pores in the structure through proton bridges. The protons (not shown for the sake of clarity) on the free carboxylic units (see circles) can be exchanged by lithium (or sodium) ions following a relatively simple ion exchange procedure. b) View along the c -axis; gray areas illustrate the diffusion channels. c) Perspective view to highlight the channel structure of MIL-121 and the 1D diffusion pathways along the c -direction.

2.2. Li^+ and Na^+ Conductivity in MIL-121 Hybrid Electrolytes

The ionic conductivity measurements revealed that both Li^+ and Na^+ ions are mobile in the modified MIL-121 samples soaked with a liquid electrolyte. **Figure 3a** shows the Nyquist plot of both MIL-121/Li and MIL-121/Na soaked with their corresponding electrolytes (soaking electrolyte (SE)). Note that they differ in the loading of SE: MIL-121/Na+SE contains 50 wt% of SE, while MIL-121/Li+SE contains only ≈ 30 wt%.

Analyzing the semicircles seen on the Nyquist plot of the functionalized MIL-121/Na(Li)+SE samples (**Figure 3a**) and fitting them with an appropriate equivalent circuit, which was composed of a resistance (R) connected in parallel to a constant phase element (CPE), yielded capacitances C in the order of 17 pF. In general, values in the pF range clearly reveal that the electrical relaxation process seen in the complex plane plot is caused by bulk processes.^[30] Notably, the CPEs of both responses used to simulate the data almost behave as ideal capacitors because their n values are close to 1; in such cases the center of the semicircle do almost coincide with the Z' axis. The resistance of the pellet under investigation was directly read off from the intercept of the location curve with the Z' axis, see vertical arrows in **Figure 3a**. Here, we converted the Z' values from the intercept into specific conductivities. The so-called DC conductivities, which refer to the frequency-independent regions in

the corresponding conductivity isotherms (see **Figure S4**, Supporting Information), are plotted in **Figure 3b** using an Arrhenius representation $\sigma_{\text{DC}}T \propto \exp(-E_a/k_B T)$; k_B denotes Boltzmann's constant. We recognize that at low temperatures $\sigma_{\text{DC}}T$ strongly depends on T . In this regime, which we call regime I, activation energies of $E_a = 1.01(2)$ eV and $E_a = 1.23(3)$ eV, respectively, were obtained (see **Figure 3b**).

At $\vartheta = 10$ and 50 °C, we recognize that the Arrhenius line passes through kinks leading to a temperature regime for which $\sigma_{\text{DC}}T$ is much less thermally activated. In this region (regime II), which starts at $\vartheta = 10$ °C for the MIL-121/Na+SE sample, E_a drastically decreases from 1.23 to 0.36 eV. For MIL-121/Li+SE, a decrease from 1.01 to 0.28 eV is seen. The Nyquist plots shown in **Figure 3a** refer to a temperature in this region, viz., 30 °C; it can be clearly seen that the conductivity of MIL-121/Na+SE (1.2×10^{-4} S cm^{-1}) is higher than that measured for the MIL-121/Li+SE at 30 °C (regime I). Comparing values at 50 °C, the difference is, however, only very little, viz., 2.9×10^{-4} S cm^{-1} for MIL-121/Na+SE versus 9.1×10^{-5} S cm^{-1} (MIL-121/Li+SE), see also **Figure 3b**; still the Na-bearing samples reveal a higher ionic conductivity. To explain this difference, we have to keep in mind that a higher amount of SE was added to MIL-121/Na, which increases the charge carrier concentration in this sample. Clearly, this is still inferior to liquid electrolytes; 1 M NaClO_4 in propylene carbonate (PC) reaches 6 mS cm^{-1} and 1 M LiClO_4 in

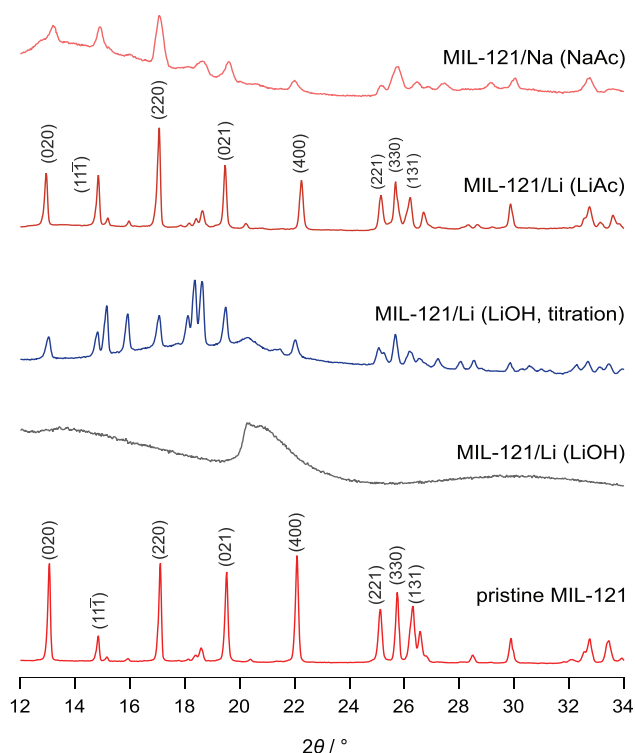


Figure 2. XRD powder diffraction patterns of lithiated and sodiated MIL-121 (top). To find out an appropriate procedure for lithiation and sodiation of MIL-121, different approaches were carried out and the results were evaluated by XRD. The analyzed approaches include modifications with LiOH, titration with LiOH, lithiation with LiAc, and sodiation with NaAc, as indicated. *hkl* indices are added to the main reflections of pristine MIL-121, which is shown as a reference.

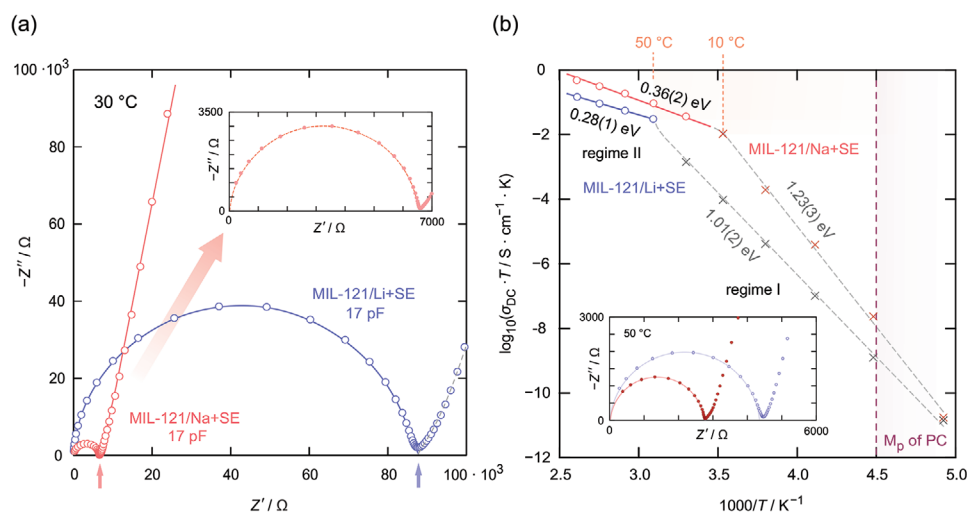


Figure 3. a) Nyquist plots, recorded at 30 °C, of MIL-121/Li+SE (containing 30 wt% of SE) and MIL-121/Na+SE (containing 50 wt% of SE). The lines drawn are to guide the eye. The inset shows a magnification of the location curve of MIL-121/Na+SE. b) Arrhenius plot of the so-called DC conductivity of the two functionalized MOF samples. The inset shows the Nyquist plot of two curves recorded at 50 °C. Starting at low temperatures, the ionic conductivity is rather low and characterized by activation energies as high as 1 and 1.2 eV, respectively. For both samples, a kink is seen at 50 and 10 °C, respectively, above which the values of ionic conductivities are as high as 0.1 mS cm⁻¹. The corresponding activation energies E_a decrease to 0.28 and 0.36 eV, respectively. We explain this behavior by a crossover from correlated (regime I) to weakly correlated (uncorrelated) motion (regime II). Activation energies of the order of 0.28 eV are close to those expected for an elementary hop. See the text for further explanation.

PC 5 mS cm⁻¹ at 25 °C.^[31] Yet, the obtained ionic conductivities are in line with other MOF-based electrolytes.^[23]

To evaluate the importance of the interaction between the modified MIL-121 and the liquid electrolyte, we measured reference samples where one of the components is missing. First, we saw that modifying MIL-121 with lithium and sodium acetate does not lead to an electrically conductive MOF, which was verified by both conductivity measurements and NMR spectroscopy (see Figures 5 and 6). We suppose that the ions are bound too strong to the carboxylic groups and that the energy barrier for a jump is simply too high.

Second, when we tested the material by soaking it in pure PC without conductive salt, we observed extremely poor conductivities. Pure PC seems to be unable to sufficiently weaken the bonding between the ions and the carboxylic groups in the modified MIL-121, see Figure S3 in the Supporting Information that indeed reveals very low conductivities. Although modified with Li⁺ or Na⁺ ions, the samples are electrical insulators at ambient conditions. To understand this, we may mention that only approximately one third of carboxylic units bear Li⁺ or Na⁺ (see Table S1, Supporting Information). In a simple approximation, a jump from one carboxylic position to the next unoccupied site implies sufficient ion solvation to break the bond with the framework, transport over a relatively long distance and, at least partial desolvation at the receiving site. Such a complex succession of steps would very likely imply a low occurrence probability. Thus, as demonstrated by conductivity data, pure PC-mediated vehicular ion transport within the porous MIL-121 structure has a negligible influence on the conductivity of the MIL-121/Li+PC and MIL-121/Na+PC materials.

Third, samples without lithium or sodium ions at the carboxylic groups but with SE, i.e., unmodified MIL-121+SE, are also

characterized by significantly lower conductivities compared to those seen for MIL-121/Li+SE and MIL-121/Na+SE; the conductivities of the unmodified samples turned out to be lower by at least four orders of magnitude (see Figure S4, Supporting Information). In these samples, the charge carrier concentration (Table S2, Supporting Information) is lower than in the modified MIL-121 powders that do not contain SE or PC. This confirms that pure vehicular ion transport in the pores is very slow and contributes almost insignificantly to the total conductivity.

From elemental analysis data (Table S1, Supporting Information), we can also determine the concentration of mobile species in the modified MIL-121 samples (Table S2, Supporting Information). We see that the concentration of Li⁺ and Na⁺ is the highest in the modified MIL-121 powders that do not contain any PC or SE. Yet, these samples are not conductive—the ionic species are largely immobile (see Figures 5 and 6). Also, the concentration of Li⁺ is roughly 6 times higher than for MIL-121+SE; however we see an increase in conductivity for MIL-121/Li+SE by four orders of magnitude. A similar situation occurs for sodium samples; an increase of 4.5 times in Na⁺ concentration leads to a conductivity that is again four orders of magnitude higher. This illustrates the importance of the mobility parameter of ionic species—our successful modification strategy leads to high conductivity because the mobility of the ionic species is greatly enhanced.

Furthermore, we conclude that the interaction between the modified MIL-121 and the SE creates a, most likely, interfacial transport pathway along the channels; the SE assists the ions to move over long distances. At low temperatures, this kind of transport is to be characterized by so-called correlated motions as will be discussed below, see also the Supporting Information. On the other hand, we see that the ionic conductivity of the SE, when residing in the pores of the MOF host structure, is significantly lower than in the pure liquid state. Hence, the SE has lost its liquid properties when present in the hybrid electrolyte prepared. Importantly, the reference samples also reveal that, in the absence of Li⁺ or Na⁺ cations, we can exclude any significant proton conduction in MIL-121.

2.3. Structural Characterization and Arrhenius Behavior in Regimes I and II

Results from TGA, DSC, and Raman Spectroscopy: As mentioned above, the activation energy in the hybrid electrolyte system increases significantly for both ion species at lower temperatures, see regime I in Figure 3b. These kinks may occur when, e.g., two temperature-activated phenomena contribute to the total conduction process.^[32] A similar trend in Arrhenius lines was found by Souquet et al. where polymer composites show a nonlinear behavior with different activation energies in different temperature regimes.^[33] Furthermore, also structural changes or phase transitions can lead to different conduction properties above and below the transition temperature.^[34] Here, in our case, structural changes or first-order phase transitions are, however, largely excluded as pristine and modified MIL-121 as well are thermally stable over the whole temperature range investigated. Moreover, no heat flow, usually associated with a first-order phase transition, is detected on lithiated and sodiated

samples, see Figures S5 and S6 in the Supporting Information. Furthermore, the melting (−49 °C) and boiling (242 °C) of propylene carbonate do not occur close to the conductivity transition regime that we observed in the Arrhenius plot. In addition, we performed differential scanning calorimetry (DSC) measurements on MIL-121/Li+SE and MIL-121/Na+SE from −60 to 100 °C (see Figure S7, Supporting Information) to exclude first- or second-order phase transitions. Again, also DSC revealed no heat flow and no indication of a sudden heat capacity change. The broad endothermic heat flow seen over the entire temperature range is due to the slow evaporation of the PC solvent. Furthermore, variable-temperature Raman spectroscopy did not reveal any substantial structural differences (Figure S8, Supporting Information). Admittedly, the materials have a high level of fluorescence, but for the Li-based MOFs background subtraction was not overly complicated and the resulting spectra turned out to be of high quality. The spectra recorded for the Li-containing MOFs did not show significant deviations at different temperatures. Only a few shifts by ≈1 to 2 cm^{−1} were observed as function of temperature. The Na-based MOFs were more difficult to analyze, but they show few if any differences as compared to the Li-based counterparts. In summary, results from Raman spectroscopy are in line with the findings from thermogravimetric analysis (TGA) and DSC measurements and prove that no structural modifications occur. This conclusion is further corroborated by variable-temperature ¹H MAS (magic angle spinning) NMR and ¹H-¹³C CP MAS NMR (see also below), which we used to characterize the sodiated sample MIL-121/Na+SE. We could not observe any difference between spectra (see Figure S9, Supporting Information) recorded above (30 °C) and below (−10 °C) the kink seen at 10 °C in Figure 3b.

Ion–Ion Interactions: The absence of any structural change or any phase transition strengthens the hypothesis that other origins are at play causing the change in transport properties. Surface or interfacial effects, including space charge effects,^[35,36] in particular, might be helpful in explaining the temperature behavior seen in Figure 3b.

In nanostructured composite materials,^[36,37] consisting of an insulating and a conducting phase, e.g., fast interfacial diffusion is reported allowing the mobile charge carriers to move faster than in the individual compounds.^[38] Here, we suspect that in analogy to other famous systems and in line with the model proposed by Ngai and co-workers,^[39,40] our $\sigma_{DC}T$ data indeed reveal a change in ion–ion interactions at the inner surface regions of the 1D channels in the functionalized MOF, see Figure 1. We assume that at higher temperatures (regime II) strong ion–ion correlation effects become less relevant for overall Li⁺ and Na⁺ ion dynamics. This assumption follows the initial phenomenological coupling model of Ngai et al.,^[40–42] which, in the meantime, has been used to explain conduction properties of a variety of different systems.^[42] Quite recently, a very similar behavior was found for Na⁺ ion conduction in the *closo*-borate Na₂(B₁₂H₁₂)_{0.5}(B₁₀H₁₀)_{0.5},^[43] for which significantly lower activation energies were found at higher temperatures. In analogy to our MOF-based systems, no strong structural changes or phase transitions occur in the *closo*-borate for which a single diffusion process is seen in both electric modulus spectroscopy and conductivity isotherms. Importantly, Na site order–disorder

effects may affect the temperature dependence of ionic conductivity. At very low temperatures, spatially restricted librations of the large anions, as observed by quasi-elastic neutron scattering, induce dynamical background energy fluctuations. Finally, Na^+ conduction of $\text{Na}_2(\text{B}_{12}\text{H}_{12})_{0.5}(\text{B}_{10}\text{H}_{10})_{0.5}$ was interpreted in the frame of the coupling model: at a certain crossover temperature ($\approx 60^\circ\text{C}$), conduction is increasingly governed by ion–ion interactions while at high temperatures random particle walks and almost noncorrelated motion dominates. These regimes are to be described by electric field relaxation functions that change from a nonexponential, i.e., stretched exponential (low T regime) to an exponential function (high T regime). In general, ion–ion interactions may originate from both self-correlations of the moving charge carriers as well as from cation–anion or cation–framework (rotational) interactions leading to nonrandom but correlated motion. Such effects affect the conductivity isotherms in the high-frequency regime, which is the so-called (alternating current, AC) dispersive regime. In the frame of Funke's jump relaxation model,^[44] such correlated motions include fast forward-and-backward jump processes on a more or less local length scale that do not lead to long-range ion transport.

A similar change in conductivity behavior was observed by Briant and Farrington who attributed the kink in the Arrhenius conduction behavior of $\text{Na}-\beta'$ -alumina to an ordered configuration of the mobile ions that might built up at lower temperatures.^[45] Later Funke explained this kink in terms of his famous jump relaxation model.^[46] At low temperatures, only a small fraction of successful jumps contribute to the DC conductivity plateau. This situation resembles an ionic conductor with a very low concentration of charge carriers. At low temperatures and low measuring frequencies, slow rearrangement processes of the neighborhood of the Li^+ (Na^+) ions cause the ions to mainly jump forward and backward. Most likely, here we sense such spatially restricted (cage-like) dynamic processes in the nearly constant loss (NCL) dispersive part of the conductivity isotherms of MIL-121/Li(Na)+SE, see Figure S4 in the Supporting Information. Above the NCL-regime, our isotherms reveal a classical dispersive regime with a Jonscher exponent^[47] p of 0.66 pointing to correlated ion dynamics in regime I, see Figure S4 in the Supporting Information. The exponent is a measure of the ion–ion interactions being present. Noteworthy, as in the case of the *closo*-borate $\text{Na}_2(\text{B}_{12}\text{H}_{12})_{0.5}(\text{B}_{10}\text{H}_{10})_{0.5}$,^[43] the shape of both the conductivity isotherms (Figure S4, Supporting Information) and electric modulus data of MIL-121/Li(Na)+SE point to a single transport process in our system.

Coming back to $\text{Na}-\beta'$ -alumina, above the crossover temperature of 465 K the relaxation of the neighborhood becomes fast enough to inhibit any ensuing backward jumps of the ions.^[46] Fast relaxation leads to an increase of the number of successful processes as the backward jumps are no longer energetically preferred. At sufficiently high T , the thermal energy is large enough in such a way that correlation effects or energy fluctuations in the system become less relevant for the mobile ions. The corresponding activation energy in this temperature range reflects that of an elementary hopping process. Finally, two conductivity regimes are sensed depending on the frequency window of the conductivity measurements.^[46]

Here, a very similar conductivity behavior is seen. We can either explain it by i) the abovementioned competition between the jump processes and (immediate or retarded) lattice relaxation in an asymmetric potential or ii) by additional interactions, particularly including cooperative effects, coming into play at sufficiently high temperatures. Of course, the latter may also facilitate the rearrangement of the $\text{Li}^+(\text{Na}^+)$ surroundings at higher T , thus lowering E_a . At low temperatures, only a fraction of the elementary steps are successful leading to a decrease in σ_{DC} and to an increase in activation energy. As mentioned above, the activation energy in regime II (0.28 eV for MIL-121/Li+SE) would correspond to that of an elementary hop. Here, the difference $1.01 - 0.28 \text{ eV} = 0.73 \text{ eV}$ is regarded as the energy required for the rearrangement of the ionic neighborhood.^[46] For MIL-121/Na+SE, a value of 0.87 eV is obtained. Most likely, as Na^+ is expected to be less tightly bond to the MOF host because of its larger polarizability compared to Li^+ , the crossover temperature is lower for MIL-121/Na+SE although we observed a higher rearrangement energy. According to Ngai's model, the activation energies of the two regimes are connected to each other via $E_a(\text{regime II}) = (1 - n)E_a(\text{regime I})$ yielding $n = 0.72$ for MIL-121/Li+SE; this value is in close agreement with the Jonscher exponent found in the dispersive conductivity regime ($p = 0.66$), Figure S4 (a) in and the Supporting Information. For MIL-121/Na+SE, a very similar agreement is found: $n = 0.71$; $p = 0.64$, see Figure S4 (b) in the Supporting Information.

Considering the nature of correlation effects in the system studied here, we may think about a variety of origins. As mentioned above, only the combination of modified MIL-121/Li(Na) with SE yields this effect, for which we think the interaction between the Li(Na)-bearing host and the SE is crucial to explain the motion along the 1D channels in the pores. Indeed, free carboxylic groups, lining the channels on two sides, have part of their acidic protons exchanged with lithium or sodium cations, see Figure 1. Thus, it is plausible to consider that, above a certain temperature, conductive pathways open-up along these units. Likely, PC partially solvate the cations on the carboxylic groups, thus, lowering the transition temperature. Without knowing the exact interplay of the teammates (carboxylic $\text{Li}^+(\text{Na}^+)$, H^+ , the carboxylic groups themselves, the solvent molecules, $\text{Li}^+(\text{Na}^+)$ of PC), we suppose that cation–cation interactions, cation–anion interactions, and/or translational–rotational couplings are at play that determine the (interfacial) ion transport in MIL-121/Li(Na)+SE, see Figure 3b. In some cases, as has been shown for garnet-type ionic conductors, e.g., these effects may result in a rather flat energy landscape with many available sites connected by low activation energies.^[48] A similar situation has recently been found in $\text{LiTi}_2(\text{PS}_4)_3$.^[49] These features lead to frustrated energy landscapes that allows for concerted motions. In such a case, the backward jumps seem to play only a minor role.

In addition, rotational motions may result in cooperative motions enabling the ions to easily jump from site to site. In favorable cases, a sequence of them will result in macroscopic transport. Combining MIL-121/Li(Na) with SE seems to provide such a flat (interfacial) potential landscape with multiple sites being accessible by the ionic charge carriers along the MOF channels.

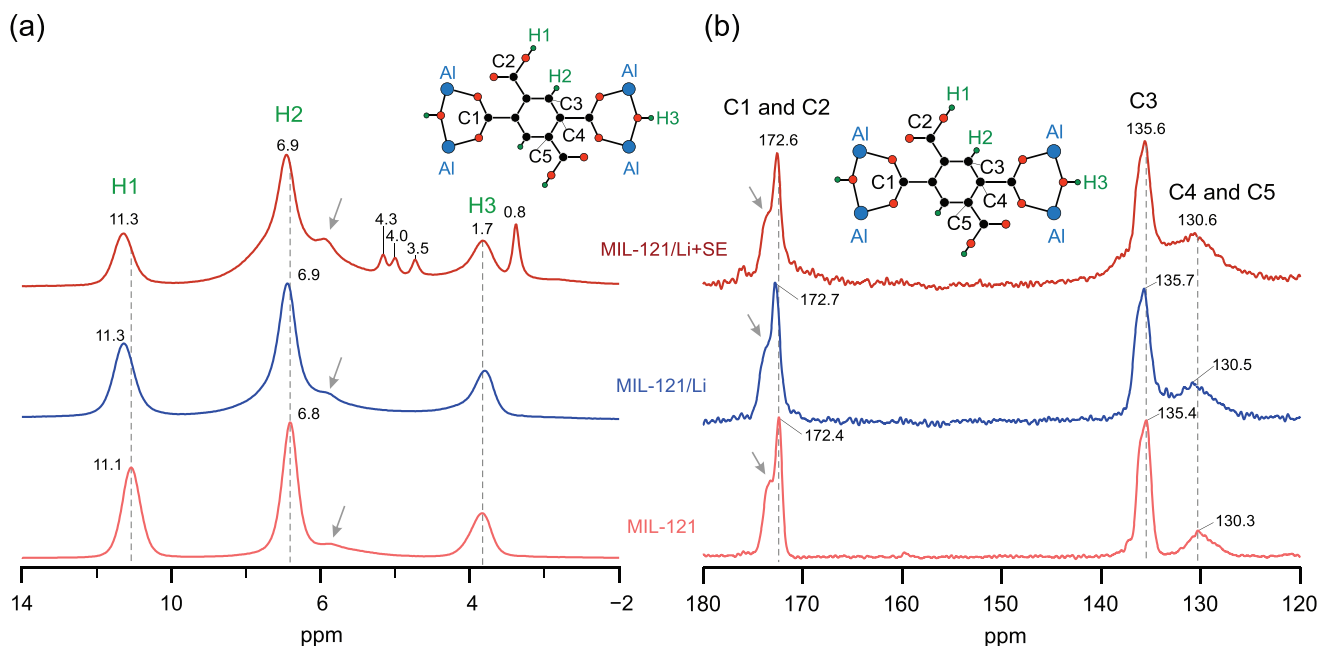


Figure 4. a) ^1H MAS NMR spectra and b) ^1H - ^{13}C CP MAS NMR spectra of MIL-121, MIL-121/Li, and MIL-121+SE (10 ms contact time). Spectra were recorded at ambient bearing gas temperature, thus, they refer to temperature regime II. Spectra were scaled such that the main signals show the same intensity. Values indicated denote isotropic chemical shifts. The insets illustrate the assignments of the NMR lines to the respective C and H atoms in MIL-121.

^1H and ^{13}C MAS NMR: As already mentioned above, to further investigate the (interfacial) environment of the Li^+ and Na^+ ions in the MOFs, we used ^1H and ^{13}C MAS NMR (Figure 4, see also Supporting Information) to directly characterize any change of the organic host structure of the MOFs upon modification and soaking with electrolyte. The spectra recorded here for MIL-121 and MIL-121/Li are in good agreement with those presented earlier (see Figure S10, Supporting Information),^[50,51] but noteworthy, our spectra have better resolution than those presented in the literature so far.

As an example, in Figure 4 the ^1H and ^1H - ^{13}C CP MAS spectra of MIL-121, MIL-121/Li, and MIL-121/Li+SE are shown. The assignment of the NMR lines follows the suggestion of Chen et al.^[51] The H1 atom (11.1 ppm) is assigned to that of the carboxylic group; upon lithiation its NMR line slightly shifts toward positive values by 0.2 ppm. Soaking with electrolyte does not change its isotropic chemical shift value further. Importantly, for spectra fully recovered with regard to spin-lattice relaxation, the intensity of the H1 NMR line decreased upon lithiation, proving that the H1 position is partly exchanged by Li^+ ; here, the relative intensities of the H1 signal are 0.67 (MIL-121), 0.57 (MIL-121/Li), and 0.43 (MIL-121/Li+SE), respectively. This observation is in line with a study on MIL-121/Na which also showed a decreased intensity of the H1 line upon modification compared to pristine MIL-121^[50] (see Figure S10, Supporting Information).

The H2 NMR line also experiences a slight shift on the ppm scale, which can be interpreted as deshielding effect of the acidic protons mediated by the carboxylic groups with which Li^+ is interacting. As a hard Lewis acid, Li^+ is expected to reduce the electron density of these groups. Interestingly, the shoulder occurring at the H2 position (see arrows in Figure 4a) rises in its relative intensity from the activated MIL-121 to the lithiated form and reaches its maximum after soaking with SE. The

origin of this change is still unknown; it might be related to protons directly interacting with Li^+ and the solvent molecules. Finally, the samples equipped with the soaking electrolyte reveal additional signals at 4.3, 4.0, 3.5, and 0.8 ppm, which we assign to PC. In contrast to H1 and H2, the NMR line belonging to H3 does not experience any influence upon both the lithiation and the addition of SE.

The ^1H - ^{13}C CP MAS spectra (Figure 4b), optimized in terms of contact time (see Figure S11, Supporting Information), reveal a similar picture in terms of line shifts as seen by ^1H MAS NMR. Lithiation and/or addition of SE cause the isotropic shifts of all C to slightly shift toward more positive ppm values. At first glance, any change in the NMR signal belonging to C1/C2 turned out to be rather small. Nevertheless, in contrast to Chen et al., who detected only one combined, but asymmetric, signal for the two C atoms,^[50,51] we were able to resolve this signal even for the unmodified MIL-121. Next to the NMR line at 172.4 ppm, a relatively prominent shoulder appears, which changes upon lithiation. We tend to attribute this shoulder to the carboxylic C2 position that experiences Li^+ in its direct vicinity. Upon lithiation, the shoulder gains slightly in intensity and broadens. Furthermore, an increase in intensity of the signals assigned to C4 and C5 (130.3 ppm), respectively, was found when comparing the activated MIL-121 with its lithiated form. A further increase in relative intensity is seen for the MIL-121/Li+SE sample. The latter change clearly reflects the influence of electrolyte on these C atoms resulting in a broader distribution of chemical shifts.

To underscore the assignment presented in Figure 4, we also investigated an “over-activated” MIL-121 sample that was heat-treated at 400 °C (see Figure S10, Supporting Information). For this sample, the H1 signal almost vanishes and a new signal appears in ^1H - ^{13}C CP MAS NMR pointing to the formation of

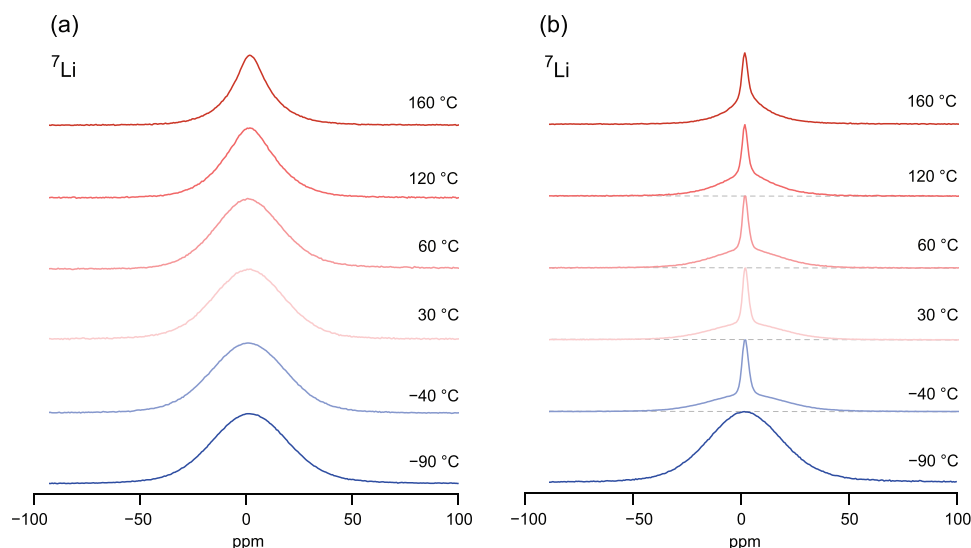


Figure 5. ^7Li NMR lines of a) MIL-121/Li and b) MIL-121/Li+SE recorded at temperatures ranging from -90 to 160 °C. Above the melting point of PC, a sharp, motionally narrowed line on top of the broad component is seen for SE MIL-121/Li+SE. Above 30 °C, this line is expected to reflect the Li^+ ions that are responsible for the high (long-range) ion conductivity, see Figure 3.

the corresponding anhydride.^[51] Additionally, a humid sample was studied to prove that the samples investigated are free of any water residuals. Indeed, the ^1H MAS NMR spectrum of the humid sample, and to some extent also that of the nonactivated (as prepared) MIL-121, revealed signals which we assign to H_2O molecules.

Finally and for the sake of completeness, we analyzed the MOF samples via ^{27}Al MAS NMR. ^{27}Al MAS NMR did not show significant changes when going from MIL-121 to the lithiated and soaked samples; hence, we conclude that the Al atoms are not affected by lithiation or addition of SE (Figure S11b, Supporting Information). The corresponding quadrupolar perturbed ^{27}Al NMR central lines reveal, however, that MIL-121/Na(+SE) seems to be affected by structural disorder, i.e., distortions or variations in bond lengths that influence local electric field gradients. This observation is in line with the change in broadening of the corresponding XRD reflections when comparing MIL-121/Li with MIL-121/Na, see Figure 2. The line shape of ^{27}Al MAS NMR, perturbed by second-order quadrupolar effects, was simulated to estimate the quadrupole coupling constant ($C_q = 8.3$ MHz) and the corresponding asymmetry parameter ($\eta = 0.28$).

Although ^1H and ^{13}C MAS NMR is able to provide a detailed structural picture on configurational properties of MIL-121, our results do not point to prominent structural changes, which is in agreement with Raman spectroscopy. This finding again supports our hypothesis that the change in conduction mechanism is presumably caused by a change in ion-ion interactions. To find further evidence underpinning this idea, we used ^7Li and ^{23}Na NMR spin-lattice relaxation measurements to directly probe cation dynamics on the angstrom length scale for the soaked and nonsoaked samples. Importantly, we also recorded ^1H NMR spin-lattice relaxation rates to figure out whether ^7Li or ^1H provides the main driving force in longitudinal relaxation. We find evidence that indeed Li^+ ions seem to be the main charge carriers being responsible for the conductivity regime II.

2.4. Insights into Li^+ and Na^+ Self-Diffusion by Time-Domain NMR Spin-Lattice Relaxation

The easiest way to determine Li^+ ion mobility in crystalline matter is to record static, i.e., non-MAS, NMR lines as a function of temperature. As an example, variable-temperature ^7Li NMR lines of MIL-121/Li with and without SE are shown in Figure 5. The ^7Li NMR lines of MIL-121/Li, which we recorded from -90 to 160 °C, can be described with a broad Gaussian shape at low temperatures. Narrowing of the line due to diffusive motions that average ^7Li - ^7Li dipole-dipole interactions^[52,53] turns out to start at temperatures as high as 120 °C. At this temperature, the mean correlation rate is in the order of several kHz as its magnitude is given by the line width in the rigid lattice regime (5.0 kHz).

The same line is also seen for MIL-121/Li+SE (see Figure 5b); at -40 °C, however, the line undergoes significant narrowing which we ascribe to the melting of PC (melting point -49 °C). Hence, the superimposed narrow line represents Li^+ ions in the liquid phase that are exposed to strong spin fluctuations either caused by rotational or translational dynamics. With increasing temperature, the sharp line remains almost unchanged whereas the broad line starts narrowing. Above 50 °C, the conductivity of MIL-121/Li+SE enters regime II, see Figure 3. We assume that in this temperature range, carboxylic Li^+ ions participate in long-range diffusion along the MOF channels. Presumably, as the ^7Li line shape does not change when going from 30 to 60 °C, this diffusion process also involves rapid exchange with the Li^+ ions of the liquid phase.

A similar behavior was found for the Na-bearing samples, see Figure S12 in the Supporting Information that shows spectra recorded under MAS conditions (25 kHz rotation speed). Again, we observed only little motion-induced line narrowing in the nonsoaked sample and two clearly distinguishable NMR components in the spectra of MIL-121/Na+SE. As compared to ^7Li , the ^{23}Na line shape is asymmetric; it is perturbed by second

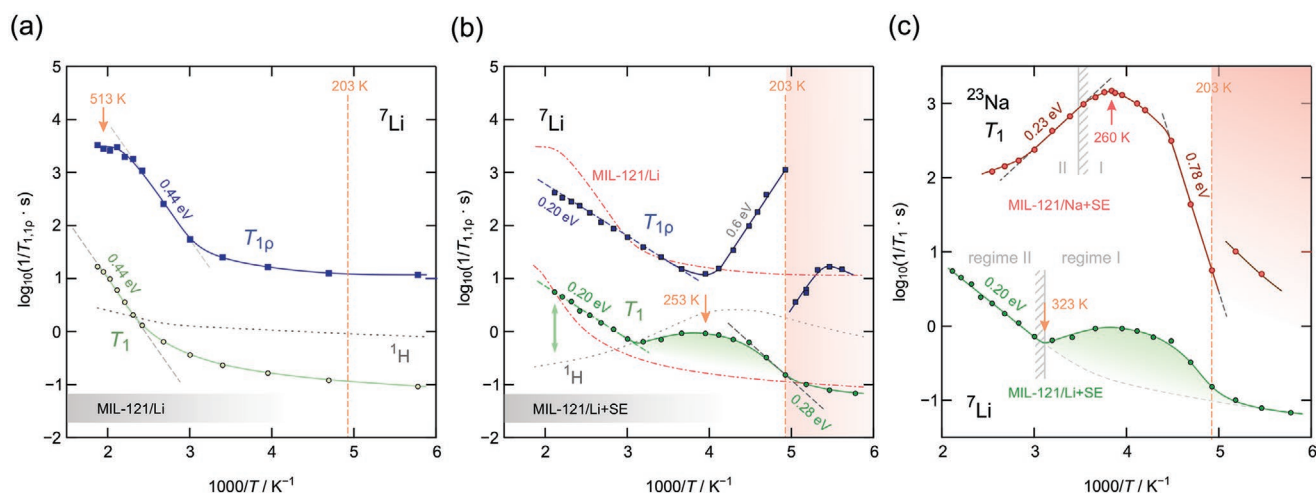


Figure 6. ${}^7\text{Li}$ NMR spin-lattice relaxation rates of a) MIL-121/Li and b) MIL-121/Li+SE. In (c), the ${}^{23}\text{Na}$ NMR rates $1/T_1$ of MIL-121/Na+SE are shown. While in MIL-121/Li Li^+ relaxation is governed by an activation energy of 0.44 eV, for MIL-121/Li+SE this value has decreased to 0.20 eV. The local maximum at $T = 253$ K, see (b), reflects ${}^7\text{Li}$ NMR spin fluctuations influenced by liquid PC. This relaxation source also affects ${}^{23}\text{Na}$ spin-lattice relaxation, see (c). We attribute the ${}^{23}\text{Na}$ NMR rate peak at 260 K to fluctuations in the liquid phase (regime I). The rates in regime II are influenced by this kind of spin-fluctuations as well. The dotted lines in (a) and (b) show the ${}^1\text{H}$ NMR $1/T_1$ rates, see also Figures S13 and S14a in the Supporting Information; for MIL-121/Li+SE (see (b)), they reveal the opposite behavior as ${}^7\text{Li}$ ($T > 300$ K) and indicate that Li^+ acts as the main charge carrier in the modified Li-bearing MOF, see double arrow.

quadrupolar effects, which are not averaged by standard MAS, as expected for a nucleus experiencing strong quadrupole coupling between its quadrupole moment and electric field gradients at the nuclear site.

${}^7\text{Li}$, ${}^{23}\text{Na}$ (MAS), and ${}^1\text{H}$ NMR Spin-Lattice Relaxation: To collect information on the diffusive motion of the ${}^7\text{Li}$ spins at the atomic length scale, we probed diffusion-induced $1/T_1$ and $1/T_{1\rho}$ relaxation rates,^[54] which were analyzed in the frame of an Arrhenius representation shown in **Figure 6**. In **Figure 6a**, the temperature behavior of both $1/T_1$ and $1/T_{1\rho}$ of MIL-121/Li is shown. Below $T = 330$ K, the rates are governed by non-diffusive effects as they only change little, i.e., less than thermally activated, with temperature. At elevated T , they pass into the so-called low- T flank of the diffusion-induced rate peaks they belong to. These peaks appear when the mean jump rate reaches the resonance frequency at which the rates were recorded ($\omega_{0(1)}\tau \approx 1$).^[55] As the angular spin-lock frequency ω_1 ($= 20 \text{ kHz} \times 2\pi$) is orders of magnitude lower than ω_0 ($= 116 \text{ MHz} \times 2\pi$), the $1/T_{1\rho}(1/T)$ rate peak becomes apparent at lower temperature (513 K). Importantly, the slopes of the two flanks are equal, which shows that the two methods probe the same source of spin fluctuations in MIL-121/Li.

For MIL-121/Li+SE, new features emerge in both ${}^7\text{Li}$ $1/T_1$ and $1/T_{1\rho}$ NMR. Already at $T = 253$ K, the rate $1/T_1$ passes through a shallow peak superimposing the background relaxation rates. We assign this peak to rapid Li^+ translational motions in liquid PC in MIL-121/Li+SE. The corresponding activation energy of 0.28 eV is to be regarded as a rough estimate as the peak is strongly influenced by background relaxation. For comparison, the high- T flank of the spin-lock $1/T_{1\rho}(1/T)$ rate peak, which is the so-called *corresponding* peak to that seen in T_1 NMR peak,^[55] yields 0.6 eV, see **Figure 6b**. In contrast to $1/T_1$, spin-lock $1/T_{1\rho}$ NMR is also able to probe the melting of PC as the rates abruptly decrease at $T = 203$ K by almost three orders of

magnitude. The $1/T_{1\rho}(1/T)$ rate peak seen below this temperature might be a result of fast rotational jump processes indirectly sensed by the ${}^7\text{Li}$ probes.

Li^+ or Li^+/H^+ Conduction: As discussed for MIL-121/Li, at temperatures above 330 and 280 K, respectively, the rates shown in **Figure 6b** of MIL-121/Li+SE probe the low- T flank of the main spin-rate peak that we again attribute to Li^+ translational diffusion. Most importantly, the two flanks run in parallel to each other and yield a much lower activation energy of only 0.20 eV as compared to those in **Figure 6a** (MIL-121/Li; 0.44 eV). However, at this stage we cannot exclude that the flanks reflect Li^+/H^+ interactions, which are indirectly sensed by the ${}^7\text{Li}$ probe. Hence, we recorded ${}^1\text{H}$ NMR spin-lattice relaxation rates to study any ${}^7\text{Li}$ - ${}^1\text{H}$ coupling, see dotted lines in **Figure 6b** and bold lines in **Figure S13** in the Supporting Information. Fortunately, ${}^1\text{H}$ NMR provides clear evidence that the flanks seen for MIL-121/Li (0.44 eV) and for MIL-121/Li+SE (0.20 eV) are to be regarded as directly caused by Li-Li spin fluctuations as they are completely missing in ${}^1\text{H}$ spin-lattice relaxation NMR, see **Figures S13** and **S14** in the Supporting Information. ${}^1\text{H}$ longitudinal NMR relaxation is only determined by background-influenced rates, most likely affected by the vibrational motions of the host. For MIL-121/Li+SE, the ${}^1\text{H}$ rates (and the ${}^1\text{H}$ NMR spectra, **Figure S14b**, Supporting Information) reflect motion-induced changes because of liquid PC. The ${}^1\text{H}$ NMR rates of MIL-121/Li+SE pass through almost the same local $1/T_1$ peak (253 K) as ${}^7\text{Li}$, see **Figure 6b**. Hence, we feel confident that the ${}^7\text{Li}$ NMR $1/T_1$ flank governed by 0.20 eV (see **Figure 6b**), which belongs to temperature regime II, characterizes the elementary Li^+ jump processes in MIL-121/Li+SE.

The observation that E_a from NMR turned out to be slightly lower than that of σ_{DC} reflects length-scale-dependent ion conduction in a heterogenous potential landscape. While σ_{DC} probes long-range ion transport, the low- T flanks of NMR peaks

are sensitive to short-range diffusive motions also including so-called within-site motions and local spin fluctuations. Such differences have frequently been observed for complex ion conductors.^[55,56] In the frame of Ngai's coupling concept, see Section 2.3, we would obtain a coupling parameter n according to $E_{a, \text{NMR}} = (1 - n)E_a$, if we identify 0.20 eV from NMR with the true single ion hopping barrier and E_a (regime II) with the corresponding value extracted from the high- T DC conductivity plateaus. Here, we obtain $n \approx 0.3$ indicating only weak correlation effects in this T regime.

Considering the conductivity values probed, we expect the rates to pass through a diffusion-induced maximum at higher temperatures. The fact that this maximum is seen in Figure 6a for MIL-121/Li already at lower T is because both the activation energy and the pre-factor of the Arrhenius line of the soaked and nonsoaked sample are different. The fact that the maximum in $1/T_{1\rho}$ of MIL-121/Li+SE is not seen below $T = 500$ K shows that the Arrhenius pre-factor in $1/\tau = 1/\tau_0 \exp(-E_a/(k_B T)) \propto 1/T_{1\rho}$ is much lower for this sample.

Finally, in Figure 6c, we present the ^{23}Na NMR spin-lattice relaxation rates of MIL-121/Na+SE, which were mainly recorded under MAS conditions; thus, first-order interactions are almost eliminated under these conditions. Again, we observe the melting of PC. In regime I, Na^+ diffusion is determined by an activation energy of 0.78 eV. This value is again clearly lower than that probed by conductivity measurements. Most likely, structural disorder, see the corresponding X-ray data, is responsible for this deviation. XRD reflections of MIL-121/Na+SE point to a structurally distorted or nm-sized sample. In general, we have to keep in mind that values probed by DC conductivity measurements sense long-range ion transport that also includes the contribution of grain boundary regions. In contrast to σ_{DC} , the ^{23}Na NMR rates are again influenced by short-range or localized (within-site) motions leading to apparent activation energies. As seen for MIL-121/Li+SE, the NCL behavior seen in Figure S4 in the Supporting Information would indeed imply caged-like or spatially restricted motions.

Importantly, the ^{23}Na NMR rate peak appearing at 260 K still reflects Na^+ motions in the liquid phase. Due to the strong quadrupolar effects ^{23}Na is subjected to, the corresponding ^{23}Na NMR rates turn out to be much larger than the ^7Li rates. Hence, in regime I ^{23}Na NMR spin-lattice relaxation is governed by liquid PC and masks any other carboxylic ^{23}Na spin-fluctuations. This behavior is in contrast to that seen with ^7Li NMR for which the corresponding peak at $T = 253$ K is characterized by a much smaller amplitude. The latter fact enabled us to measure the local energy barrier sensed by the Li^+ ions rather precisely. As mentioned above, a value as low as 0.20 eV turned out to be highly promising so that future modifications may lead to even higher diffusivities.

3. Summary and Conclusion

Hybrid Li^+ and Na^+ SSEs based on the MIL-121 MOF were prepared for the first time via a flexible ion exchange procedure followed by soaking with liquid electrolyte. The porous hybrid materials showed highly promising Na^+ ionic conductivities in the order of 10^{-4} S cm^{-1} at room temperature. As a function

of temperature, the Arrhenius plots of MIL-121/Li+SE and MIL-121/Na+SE conductivity data reveal a drastic reduction in activation energy from ≥ 1 to 0.28 eV and 0.36 eV, respectively. We attribute this change in conduction mechanism to a transition from correlated dynamics (low T), influenced by the solvent molecules and the MOF structure, to almost uncorrelated cation dynamics of the Li^+ ions residing near the functionalized carboxylic groups arrayed along the 1D pores of the MOF.

The low activation energy for Li^+ determined by conductivity measurements (0.28 eV) is fully supported by the activation energy extracted from variable-temperature ^7Li NMR spin-lattice measurements (0.20 eV). NMR measurements reveal that the activation energy for elemental Li^+ hopping is reduced by more than a factor of 2 upon adding the SE: from 0.44 eV (MIL-121/Li) to 0.20 eV (MIL-121/Li+SE). In addition, the ^1H NMR unambiguously shows that indeed the Li^+ is responsible for ionic conductivity and not the protons.

Furthermore, as no appreciable conductivity is seen for i) the lithiated or sodiated framework with dry or solvent-filled pores and ii) for the pristine activated MOF only soaked with the electrolyte, our results clearly reveal the important interplay of the solid conducting MOF framework and the soaking electrolyte inside the pores. Such interfacial effects lead to high Li^+ conductivities that can compete with those of state-of-the-art ceramic SSEs. In contrast to the more conventional SSEs, the here presented hybrid SSEs offer a manifold of possibilities to further adjust these dynamic parameters.

4. Experimental Section

Preparation of the MIL-121/Li and MIL-121/Na Hybrid Electrolytes: The hydrothermal synthesis of MIL-121 was done in a Teflon beaker enclosed in a stainless steel autoclave. After stirring the solution of aluminum nitrate nonahydrate $[\text{Al}(\text{NO}_3)_3 \cdot 9\text{H}_2\text{O}]$, pyromellitic acid ($\text{H}_4\text{btec} = 1,2,4,5\text{-benzenetetracarboxylic acid}$) and deionized water (≈ 50 mL), the mixture was heated with a rate of 4 $^\circ\text{C min}^{-1}$ and kept at 210 $^\circ\text{C}$ for 24 h. After natural cooling, a white crystalline powder was obtained.^[28] Separation of the white product from the clear yellow supernatant was done by centrifugation including several washing steps with deionized water. After drying at 80 $^\circ\text{C}$ and activation at 300 $^\circ\text{C}$ at 10^{-3} mbar under vacuum, MIL-121 was dispersed by stirring in different aqueous solutions of lithium hydroxide (1 M), lithium acetate (1 M), and sodium acetate (1 M) overnight. Via this, so-called, post-synthetic modification, Li^+ and Na^+ ions were introduced to MIL-121 by ion exchange. The morphology of pristine MIL-121 and modified MIL-121/Li was characterized by SEM; the corresponding images are shown in Figure S1 in the Supporting Information.

In a second approach, a 0.1 M solution of LiOH in deionized water was added dropwise while controlling the pH value of the suspension with a pH-meter to keep the pH-value below 10. Before each step of LiOH addition, the suspension was stirred for 5 min to distribute LiOH and to stabilize the pH-value; details on the pH stability are given in the Supporting Information. All samples were separated from the liquid through centrifugation and dried at 80 $^\circ\text{C}$. The final products appeared as yellow powders and showed a change in color from yellow to brown after activation at 300 $^\circ\text{C}$ in vacuum at 10^{-6} mbar, see Figure S1 in the Supporting Information. The samples were transferred to an Ar-filled glove box and stored in the glove box, whose atmosphere was almost free of any water or oxygen (both levels were below 0.5 ppm).

Finally, the materials were soaked with a liquid electrolyte, further referred to as SE. A 1 M solution of LiClO_4 in PC and 1 M NaClO_4 in PC acted as SE, respectively. For better homogenization, the two

components were thoroughly mixed and kept at 60 °C over night to evenly distribute the liquid throughout the pores of the solid, hence the soaking time was 14 h. All soaking steps were carried out under protective atmosphere. The limit of SE addition was roughly at 50 wt% of SE for both Li- and Na-bearing samples with respect to the modified MIL-121. Above 50 wt%, the liquid SE got pressed out of the pores during pelletizing the samples for conductivity spectroscopy measurements. Regarding the mechanical properties of the pressed samples, which were relatively brittle, values of ≈30 and 50 wt% of SE for lithium and sodium samples, respectively, lead to mechanically stable pellets. Thus, we used these lithium and sodium SE contents. Why the optimum lithium SE content was close to 30 wt%, whereas for sodium the optimum SE content was close to 50 wt% is not fully understood.

Materials Characterization: XRD, DSC, TGA, SEM, and Elemental Analysis: The samples were characterized by XRD using a Bruker D8-Advance diffractometer equipped with a Lynxeye detector (Cu K_{α} radiation (1.5406 Å)). A 2θ -range of diffraction angles was covered from 10 to 100° 2θ with a step size of 0.02° 2θ . The duration per step was varied from 2 to 4 s. All samples were measured under ambient conditions. DSC measurements, TGA, and SEM are given in the Supporting Information. SEM images showed crystallites having the expected habitus for the anisotropic MIL-121 host. Elemental analysis was carried out using inductively coupled plasma mass spectrometry (Agilent 7700); a microwave heated pressurized autoclave digestion system (Ultraclave IV, MLS ICPMS 7700x Agilent Technologies) was used. To prepare the samples, an aliquot (0.02 g) of the samples was mixed with 5 mL HNO_3 heated in the MLS UltraClave; the temperature program was as follows: ramped in 30 min to 250 °C and then heated for 30 min at 250 °C. Details are given in the Supporting Information, see Table S1 in the Supporting Information.

Raman Spectroscopy: Raman spectroscopy was performed using a Bruker Multi-RAM FT-Raman spectrometer equipped with a nitrogen-cooled germanium detector, a Nd-YAG (1064 nm) laser line was used at an operating power of 230 to 400 mW. Each Raman spectrum was derived from 55 min accumulation time (≈2000 scans) in the range of 0 to 4000 cm^{-1} with a resolution of 2 cm^{-1} . The analysis was focused on the range of 200 to 2000 cm^{-1} , where most of the important peaks appeared. The Raman spectra presented were baseline-corrected. Before carrying out the experiments above, an optimization step was performed to overcome the huge fluorescence of the samples. First, laser lines in the visible range (633 and 488 nm) were used and second, photobleaching the sample for several hours was tested, but neither reduced the fluorescence. Subsequently, the 1064 nm line in the FT-Raman spectrometer was used. The temperature of the sample was controlled using a Linkam stage cell, integrated with the spectrometer, using nitrogen flow as a cooling liquid. Due to the sensitivity of the samples to moisture, the Linkam cell was prepared inside an Ar-filled glovebox. The temperature was stepped by 10 °C between –20 and 80 °C, with a ramp of 10 °C min^{-1} , and held 55 min at each step while recording the Raman spectra.

Conductivity Spectroscopy: For the ion conductivity measurements, the samples were first pressed into pellets (5 mm in diameter) with a load of 0.3 ton, see Figure S1 in the Supporting Information. The effect of pressing on X-ray diffraction pattern is shown in Figure S2 in the Supporting Information; the host structure of the MOF was almost preserved. The resulting pellets with a thickness between 0.5 and 1.3 mm were plasma coated (Leica sputter coater EM, ACE200) with ion blocking gold layers of 100 nm on both sides. Finally, the Au-sputtered pellets were assembled in coin cells to guarantee protective atmosphere throughout the whole measurement. All steps, including coin-cell encapsulation, were carried out in the glovebox under Ar atmosphere. A Concept 80 system (Novocontrol) with an Alpha-A impedance analyzer in combination with an active ZGS sample cell was used for the measurements. Measurements covered a temperature range from –90 to 110 °C; the frequency was varied from 10 MHz to 10 mHz (100 mV amplitude). The raw data were fitted with ZView software by using an equivalent circuit consisting of a CPE and a resistor connected in parallel. Capacitances C were calculated according to $C = R^{(1-n)/n} \times Q^{1/n}$. R is the

resistance in Ω and Q has the numerical value of the admittance at $\omega = 1 \text{ rad s}^{-1}$. The variable n is dimensionless and it shows the deviation of the CPE from the behavior of an ideal RC unit, for which $n = 1$.

NMR Spectroscopy: High-resolution 1H , ^{13}C , ^{23}Na , ^{27}Al MAS NMR spectra on the Li bearing samples were recorded to collect structural information (Bruker Avance III 500 spectrometer, 11.4 Tesla magnet). Bruker 2.5 mm MAS probes was used that was operated at a spinning speed of 25 kHz. MAS rotors were filled with appropriate tools where the powder was hand-pressed firmly into the rotors. Preparing all NMR samples was strictly carried out under Ar atmosphere. While 1H , ^{27}Al , and ^{23}Na MAS NMR spectra were recorded with a single pulse experiment, a standard cross polarization (CP) pulse sequence was used to acquire ^{13}C - 1H MAS NMR spectra. The spectra were referenced with benzoic acid as a secondary reference, which was originally referenced to tetramethylsilane. The chemical shift values of ^{27}Al MAS NMR spectra were referenced to crystalline $\gamma-Al_2O_3$, here again serving as a secondary reference. The corresponding resonance frequencies were 500.00 MHz for 1H , 125.72 MHz for ^{13}C , and 130.29 MHz for ^{27}Al . For detailed information about measurement parameters, see Table S3 in the Supporting Information. For comparison, additional reference samples were prepared. First, a sample of pristine MIL-121 was activated at 400 °C before heat-treated again at 300 °C. Second, another sample was kept in H_2O saturated atmosphere in a closed container for 4 days to obtain a water-saturated MIL-121 sample, see the Supporting Information.

To probe cation self-diffusivity of the functionalized MOFs, variable-temperature 7Li , ^{23}Na (MAS), and 1H NMR spectra as well as NMR (in the case of 7Li also spin-lock) spin-lattice relaxation rates were recorded. Broadband (MAS) probes (Bruker (^{23}Na , MAS), NMR-Service (1H , ^{19}F probe, non-MAS)) were used to extend the temperature range of the MAS probe which was used to record the ^{23}Na spectra. Measurements, performed under non-MAS conditions, were carried out with a Bruker Avance III 300 spectrometer connected to a 7.0 Tesla (1H (300.00 MHz), 7Li (116.59 MHz), ^{23}Na (79.35 MHz)). For some 7Li NMR measurements, advantage of a ceramic probe (Bruker) was taken to reach the temperatures of up to 350 °C. Approximately 20 mg of sample was carefully hand-pressed in a Duran NMR tube with separators above and below the sample under Ar atmosphere; subsequently the samples were fire-sealed to permanently protect them from moisture. The well-known saturation recovery pulse sequence was applied to measure longitudinal $1/T_1$ rates; the spin-lock sequence was used to record diffusion-controlled $1/T_{1\rho}$ rates in the so-called rotating frame of reference (20 kHz locking frequency).^[52,57] The detailed information on the measurement parameters is given in Tables S3 and S4 in the Supporting Information.

Supporting Information

Supporting Information is available from the Wiley Online Library or from the author.

Acknowledgements

The authors thank Professor W. Gössler and S. Meschnark for the elemental analysis (Karl Franzens University Graz). Furthermore, the authors thank Brigitte Bitschnau for XRD and Josefine Hobisch for TGA and DSC measurements. Financial support by the Deutsche Forschungsgemeinschaft (DFG WI3600 4-1 and HA6966 1-2), the Austrian Federal Ministry of Science, Research and Economy (BMBWF), and the National Foundation for Research, Technology and Development is gratefully acknowledged. In addition, the study received considerable funding from the European Union's Horizon 2020 research and innovation program under the grant agreement no. 769929. The authors also thank the FFG (K-project Safe Battery—grant no. 856234 and project SolaBat—grant no. 853627) for financial support as well as the Swedish Energy Agency (grant no. P39909-1) and Chalmers Areas of Advance: Materials Science.

Conflict of Interest

The authors declare no conflict of interest.

Data Availability Statement

Research data are not shared.

Keywords

conductivity spectroscopy, ion dynamics, lithium ion conductors, metal-organic frameworks, sodium ion conductors, solid-state batteries

Received: November 11, 2020

Revised: January 18, 2021

Published online:

- [1] F. X. Wu, J. Maier, Y. Yu, *Chem. Soc. Rev.* **2020**, *49*, 1569.
- [2] a) P. G. Bruce, S. A. Freunberger, L. J. Hardwick, J. M. Tarascon, *Nat. Mater.* **2012**, *11*, 19; b) Y. C. Lu, B. M. Gallant, D. G. Kwabi, J. R. Harding, R. R. Mitchell, M. S. Whittingham, Y. Shao-Horn, *Energy Environ. Sci.* **2013**, *6*, 750; c) D. Larcher, J. M. Tarascon, *Nat. Chem.* **2015**, *7*, 19.
- [3] a) M. Armand, J. M. Tarascon, *Nature* **2008**, *451*, 652; b) J. Liu, Z. N. Bao, Y. Cui, E. J. Dufek, J. B. Goodenough, P. Khalifah, Q. Y. Li, B. Y. Liaw, Y. Liu, A. Manthiram, Y. S. Meng, V. R. Subramanian, M. F. Toney, V. V. Viswanathan, M. S. Whittingham, J. Xiao, W. Xu, J. H. Yang, X. Q. Yang, J. G. Zhang, *Nat. Energy* **2019**, *4*, 180.
- [4] a) J. B. Goodenough, K. S. Park, *J. Am. Chem. Soc.* **2013**, *135*, 1167; b) J. B. Goodenough, Y. Kim, *Chem. Mater.* **2010**, *22*, 587; c) M. S. Whittingham, *MRS Bull.* **2008**, *33*, 411; d) M. S. Whittingham, *Chem. Rev.* **2004**, *104*, 4271.
- [5] Z. Zhang, Y. Shao, B. Lotsch, Y.-S. Hu, H. Li, J. Janek, L. F. Nazar, C.-W. Nan, J. Maier, M. Armand, L. Chen, *Energy Environ. Sci.* **2018**, *11*, 1945.
- [6] Q. Zhao, S. Stalin, C. Z. Zhao, L. A. Archer, *Nat. Rev. Mater.* **2020**, *5*, 229.
- [7] a) Y. H. Xiao, Y. Wang, S. H. Bo, J. C. Kim, L. J. Miara, G. Ceder, *Nat. Rev. Mater.* **2020**, *5*, 105; b) E. Irisarri, A. Ponrouch, M. R. Palacin, *J. Electrochem. Soc.* **2015**, *162*, A2476; c) A. Ponrouch, D. Monti, A. Boschini, B. Steen, P. Johansson, M. R. Palacin, *J. Mater. Chem. A* **2015**, *3*, 22; d) A. Ponrouch, E. Marchante, M. Courty, J. M. Tarascon, M. R. Palacin, *Energy Environ. Sci.* **2012**, *5*, 8572; e) P. Knauth, *Solid State Ionics* **2009**, *180*, 911; f) V. Thangadurai, S. Narayanan, D. Pinzar, *Chem. Soc. Rev.* **2014**, *43*, 4714.
- [8] J. C. Bachman, S. Muy, A. Grimaud, H. H. Chang, N. Pour, S. F. Lux, O. Paschos, F. Maglia, S. Lupart, P. Lamp, L. Giordano, Y. Shao-Horn, *Chem. Rev.* **2016**, *116*, 140.
- [9] T. Krauskopf, F. H. Richter, W. G. Zeier, J. Janek, *Chem. Rev.* **2020**, *120*, 7745.
- [10] E. Quartarone, P. Mustarelli, *J. Electrochem. Soc.* **2020**, *167*, 050508.
- [11] a) T. Hosaka, K. Kubota, A. S. Hameed, S. Komaba, *Chem. Rev.* **2020**, *120*, 6358; b) Y. Lu, J. Chen, *Nat. Rev. Chem.* **2020**, *4*, 127; c) R. Rajagopalan, Y. G. Tang, X. B. Ji, C. K. Jia, H. Y. Wang, *Adv. Funct. Mater.* **2020**, *30*, 1909486.
- [12] S. Ohno, A. Banik, G. F. Dewald, M. A. Kraft, T. Krauskopf, N. Minafra, P. Till, M. Weiss, W. G. Zeier, *Prog. Energy* **2020**, *2*, 022001.
- [13] B. Dunn, H. Kamath, J. M. Tarascon, *Science* **2011**, *334*, 928.
- [14] a) M. Chen, Y. Zhang, G. Xing, Y. Tang, *Front. Chem.* **2020**, *8*, 152; b) M. H. Han, E. Gonzalo, G. Singh, T. Rojo, *Energy Environ. Sci.* **2015**, *8*, 81; c) C. Vaalma, D. Buchholz, M. Weil, S. Passerini, *Nat. Rev. Mater.* **2018**, *3*, 18013.
- [15] C. Sun, J. Liu, Y. Gong, D. P. Wilkinson, J. Zhang, *Nano Energy* **2017**, *33*, 363.
- [16] J. Janek, W. G. Zeier, *Nat. Energy* **2016**, *1*, 1.
- [17] S. Wenzel, S. Randau, T. Leichtweiss, D. A. Weber, J. Sann, W. G. Zeier, J. Janek, *Chem. Mater.* **2016**, *28*, 2400.
- [18] a) Y. Zhu, X. He, Y. Mo, *ACS Appl. Mater. Interfaces* **2015**, *7*, 23685; b) W. D. Richards, L. J. Miara, Y. Wang, J. C. Kim, G. Ceder, *Chem. Mater.* **2016**, *28*, 266.
- [19] T. K. Schwietert, V. A. Arszewska, C. Wang, C. Yu, A. Vasileiadis, N. J. J. de Klerk, J. Hageman, T. Hupfer, I. Kerkamm, Y. Xu, E. van der Maas, E. M. Kelder, S. Ganapathy, M. Wagemaker, *Nat. Mater.* **2020**, *19*, 428.
- [20] a) C. Janiak, *Dalton Trans.* **2003**, 2781; b) U. Müller, M. Schubert, F. Teich, H. Pütter, K. Schierle-Arndt, J. Pastre, *J. Mater. Chem.* **2006**, *16*, 626.
- [21] a) N. Stock, S. Biswas, *Chem. Rev.* **2012**, *112*, 933; b) M. Eddaoudi, J. Kim, N. Rosi, D. Vodak, J. Wachter, M. O'Keeffe, O. M. Yaghi, *Science* **2002**, *295*, 469.
- [22] a) X. Guan, F. Chen, Q. Fang, S. Qiu, *Chem. Soc. Rev.* **2020**, *49*, 1357; b) R. Zhao, Y. Wu, Z. Liang, L. Gao, W. Xia, Y. Zhao, R. Zou, *Energy Environ. Sci.* **2020**, *13*, 2386; c) R. Zhao, Z. Liang, R. Zou, Q. Xu, *Joule* **2018**, *2*, 2235.
- [23] a) R. Ameloot, M. Aubrey, B. M. Wiers, A. P. Gomora-Figueroa, S. N. Patel, N. P. Balsara, J. R. Long, *Chem. - Eur. J.* **2013**, *19*, 5533; b) B. M. Wiers, M. L. Foo, N. P. Balsara, J. R. Long, *J. Am. Chem. Soc.* **2011**, *133*, 14522.
- [24] A. Singh, R. Vedarajan, N. Matsumi, *J. Electrochem. Soc.* **2017**, *164*, H5169.
- [25] S. S. Park, Y. Tulchinsky, M. Dincă, *J. Am. Chem. Soc.* **2017**, *139*, 13260.
- [26] L. Shen, H. B. Wu, F. Liu, J. L. Brosmer, G. Shen, X. Wang, J. I. Zink, Q. Xiao, M. Cai, G. Wang, Y. Lu, B. Dunn, *Adv. Mater.* **2018**, *30*, 1707476.
- [27] H. Huo, B. Wu, T. Zhang, X. Zheng, L. Ge, T. Xu, X. Guo, X. Sun, *Energy Storage Mater.* **2019**, *18*, 59.
- [28] C. Volkringer, T. Loiseau, N. Guillou, G. Ferey, M. Haouas, F. Taulelle, E. Elkaim, N. Stock, *Inorg. Chem.* **2010**, *49*, 9852.
- [29] Z. Wang, J. Hu, L. Han, Z. Wang, H. Wang, Q. Zhao, J. Liu, F. Pan, *Nano Energy* **2019**, *56*, 92.
- [30] J. T. S. Irvine, D. C. Sinclair, A. R. West, *Adv. Mater.* **1990**, *2*, 132.
- [31] N. D. Cvjetanin, S. Mentus, *Phys. Chem. Chem. Phys.* **1999**, *1*, 5157.
- [32] a) F. Wu, G. Q. Tan, R. J. Chen, L. Li, J. Xiang, Y. L. Zheng, *Adv. Mater.* **2011**, *23*, 5081; b) M. A. Neouze, J. Le Bideau, P. Gaveau, S. Bellayer, A. Vioux, *Chem. Mater.* **2006**, *18*, 3931.
- [33] J. L. Souquet, M. Levy, M. Duclot, *Solid State Ionics* **1994**, *70*, 337.
- [34] a) M. Matsuo, Y. Nakamori, S. Orimo, H. Maekawa, H. Takamura, *Appl. Phys. Lett.* **2007**, *91*, 224103; b) M. Gombotz, S. Lunghammer, S. Breuer, I. Hanzu, F. Preishuber-Pflügl, H. M. R. Wilkening, *Phys. Chem. Chem. Phys.* **2019**, *21*, 1872; c) M. Yoshio, T. Mukai, H. Ohno, T. Kato, *J. Am. Chem. Soc.* **2004**, *126*, 994.
- [35] a) J. Maier, *Int. J. Mater. Res.* **2008**, *99*, 24; b) J. Maier, *Prog. Solid State Chem.* **1995**, *23*, 171.
- [36] J. Maier, *Phys. Status Solidi B* **1984**, *123*, K89.
- [37] C. C. Chen, J. Maier, *Phys. Chem. Chem. Phys.* **2017**, *19*, 6379.
- [38] a) S. Breuer, V. Pregartner, S. Lunghammer, H. M. R. Wilkening, *J. Phys. Chem. C* **2019**, *123*, 5222; b) D. Blanchard, A. Nale, D. Sveinbjornsson, T. M. Eggenhuisen, M. H. W. Verkuijlen, T. V. Suwarno, A. P. M. Kentgens, P. E. de Jongh, *Adv. Funct. Mater.* **2015**, *25*, 184; c) Y. S. Lee, Y. W. Cho, *J. Phys. Chem. C* **2017**, *121*, 17773; d) Y. S. Choi, Y. S. Lee, K. H. Oh, Y. W. Cho, *Phys. Chem. Chem. Phys.* **2016**, *18*, 22540; e) Y. S. Choi, Y. S. Lee, D. J. Choi, K. H. Chae, K. H. Oh, Y. W. Cho, *J. Phys. Chem. C* **2017**, *121*, 26209; f) R. Zettl, L. de Kort, M. Gombotz,

- H. M. R. Wilkening, P. E. de Jongh, P. Ngene, *J. Phys. Chem. C* **2020**, *124*, 2806.
- [39] K. L. Ngai, C. T. White, *Phys. Rev. B* **1979**, *20*, 2475.
- [40] K. L. Ngai, A. K. Jonscher, C. T. White, *Nature* **1979**, *277*, 185.
- [41] a) K. L. Ngai, A. K. Rizos, *Phys. Rev. Lett.* **1996**, *76*, 1296; b) E. Cuervo-Reyes, E. Roedern, Y. Yun, C. Battaglia, *Electrochim. Acta* **2019**, *297*, 435.
- [42] K. L. Ngai, R. W. Rendell, *ACS Symp. Ser.* **1997**, *676*, 45.
- [43] L. Duchene, S. Lunghammer, T. Burankova, W. C. Liao, J. P. Embs, C. Coperet, H. M. R. Wilkening, A. Remhof, H. Hagemann, C. Battaglia, *Chem. Mater.* **2019**, *31*, 3449.
- [44] a) K. Funke, *J. Non-Cryst. Solids* **1994**, *172*, 1215; b) K. Funke, *Prog. Solid State Chem.* **1993**, *22*, 111; c) K. Funke, *Solid State Ionics* **1988**, *28*, 100.
- [45] J. L. Briant, G. C. Farrington, *J. Solid State Chem.* **1980**, *33*, 385.
- [46] K. Funke, R. D. Banhatti, D. M. Laughman, L. G. Badr, M. Mutke, A. Santic, W. Wrobel, E. M. Fellberg, C. Biermann, *Z. Phys. Chem.* **2010**, *224*, 1891.
- [47] A. K. Jonscher, *Nature* **1977**, *267*, 673.
- [48] X. F. He, Y. Z. Zhu, Y. F. Mo, *Nat. Commun.* **2017**, *8*, 15893.
- [49] D. Di Stefano, A. Miglio, K. Robeyns, Y. Filinchuk, M. Lechartier, A. Senyshyn, H. Ishida, S. Spannenberger, D. Prutsch, S. Lunghammer, D. Rettenwander, M. Wilkening, B. Roling, Y. Kato, G. Hautier, *Chem* **2019**, *5*, 2450.
- [50] S. S. Chen, B. E. G. Lucier, W. Luo, X. K. Xie, K. Feng, H. Chan, V. V. Terskikh, X. H. Sun, T. K. Sham, M. S. Workentin, Y. N. Huang, *ACS Appl. Mater. Interfaces* **2018**, *10*, 30296.
- [51] S. S. Chen, S. Mukherjee, B. E. G. Lucier, Y. Guo, Y. T. A. Wong, V. V. Terskikh, M. J. Zaworotko, Y. N. Huang, *J. Am. Chem. Soc.* **2019**, *141*, 14257.
- [52] V. Epp, O. Gün, H. J. Deiseroth, M. Wilkening, *J. Phys. Chem. Lett.* **2013**, *4*, 2118.
- [53] a) M. Wilkening, V. Epp, A. Feldhoff, P. Heitjans, *J. Phys. Chem. C* **2008**, *112*, 9291; b) M. Wilkening, C. Mühle, M. Jansen, P. Heitjans, *J. Phys. Chem. B* **2007**, *111*, 8691.
- [54] a) A. Kuhn, M. Kunze, P. Sreeraj, H. D. Wiernhofer, V. Thangadurai, M. Wilkening, P. Heitjans, *Solid State Nucl. Magn. Reson.* **2012**, *42*, 2; b) A. Kuhn, S. Narayanan, L. Spencer, G. Goward, V. Thangadurai, M. Wilkening, *Phys. Rev. B* **2011**, *83*, 094302.
- [55] B. Stanje, D. Rettenwander, S. Breuer, M. Uitz, S. Berendts, M. Lerch, R. Uecker, G. Redhammer, I. Hanzu, M. Wilkening, *Ann. Phys.* **2017**, *529*, 1700140.
- [56] a) M. Wilkening, P. Heitjans, *ChemPhysChem* **2012**, *13*, 53; b) F. Preishuber-Pfögl, P. Bottke, V. Pregarner, B. Bitschnau, M. Wilkening, *Phys. Chem. Chem. Phys.* **2014**, *16*, 9580.
- [57] a) V. Epp, O. Gün, H. J. Deiseroth, M. Wilkening, *Phys. Chem. Chem. Phys.* **2013**, *15*, 7123; b) P. Heitjans, M. Wilkening, *MRS Bull.* **2009**, *34*, 915.